Supplementary Information (SI) for Journal of Materials Chemistry A.

Supporting Information

Discovery of Inaccessible Supersaturated Metastable Li_3VO_4–Li_2MoO_4 Solid Solutions via Spray Drying for High-Performance Anodes

Keisuke Matsumura[a,b], Daisuke Saito[b], Etsuro Iwama*[a,b,c], Patrick Rozier[a,d,e], Pierre-Louis Taberna[a,d,e], Patrice Simon[a,d,e], Wako Naoi[f], Katsuhiko Naoi*[a,b,c]*

[a] *Institute of Global Innovation Research, Tokyo University of Agriculture and Technology, 2-24-16 Naka-cho, Koganei, Tokyo 184-8588, Japan*

[b] *Department of Applied Chemistry, Tokyo University of Agriculture and Technology, 2-24-16 Naka-cho, Koganei, Tokyo 184-8588, Japan*

[c] *Advanced Capacitor Research Center, Tokyo University of Agriculture and Technology, 2-24-16 Naka-cho, Koganei, Tokyo 184-8588, Japan*

[d] *CIRIMAT, Université de Toulouse, CNRS, 118 Route de Narbonne, 31062 Toulouse Cedex 9, France*

[e] *Réseau sur le Stockage Électrochimique de l'Energie, RS2E FR CNRS 3459, 33 rue Saint Leu, 80039 Amiens Cedex, France*

[f] *Division of Art & Innovative Technologies, K & W Inc., 1-3-16-901 Higashi, Kunitachi, Tokyo 186-0002, Japan*

**Corresponding authors*

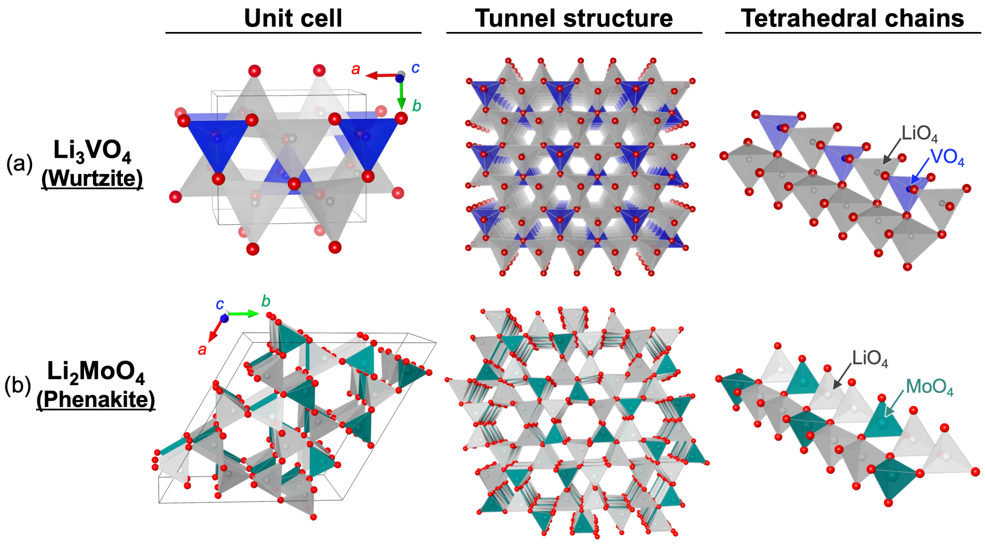

Figure S1. Crystal structures of Li_3VO_4 and Li_2MoO_4, illustrating the unit cell, tunnel framework, and tetrahedral chain connectivity. **(a)** *Li_3VO_4 (wurtzite-related framework):* The structure is constructed from two types of chains—(–LiO_4–VO_4–) and (–LiO_4–LiO_4–)—that alternate in a symmetric manner to form the crystal. The unit cell (left) shows the wurtzite-like connectivity of tetrahedra, the tunnel structure (middle) highlights one-dimensional channels extending along the c-axis, and the tetrahedral chains (right) demonstrate the alternation of LiO_4 and VO_4 units. **(b)** *Li_2MoO_4 (phenakite framework):* The structure consists of chains of the form (–LiO_4–MoO_4–LiO_4–), which are built upon the same hcp oxygen array common to Li_3VO_4. These two-chain blocks are twisted and linked; a more open tunnel framework emerges. This twisted-chain connectivity gives rise to the large c-axis channels characteristic of the phenakite structure.

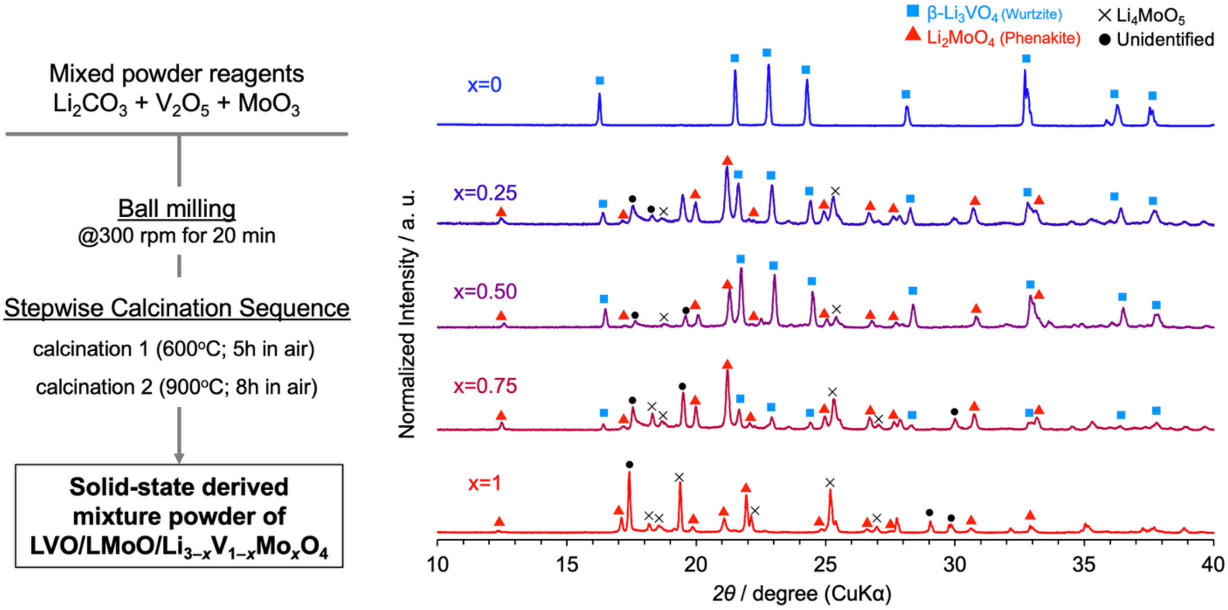

Figure S2. (Left) Schematic procedure for the solid-state synthesis of LVO/LMoO (nominal $Li_{3-x}V_{1-x}Mo_xO_4$ solid solutions) by high-temperature calcination of precursor oxides. (Right) XRD patterns of the resulting powder mixtures. Despite the straightforward thermal treatment, the targeted solid-solution phase $Li_{3-x}V_{1-x}Mo_xO_4$ did not form, as no continuous lattice shift or single-phase reflections were observed. Instead, the products contain multiple secondary phases, most notably Li_4MoO_5 together with other unidentified impurities. These results demonstrate that simple solid-state routes are insufficient to stabilize the $Li_{3-x}V_{1-x}Mo_xO_4$ solid solution, reflecting the strong tendency of V- and Mo-rich domains to segregate under equilibrium calcination conditions.

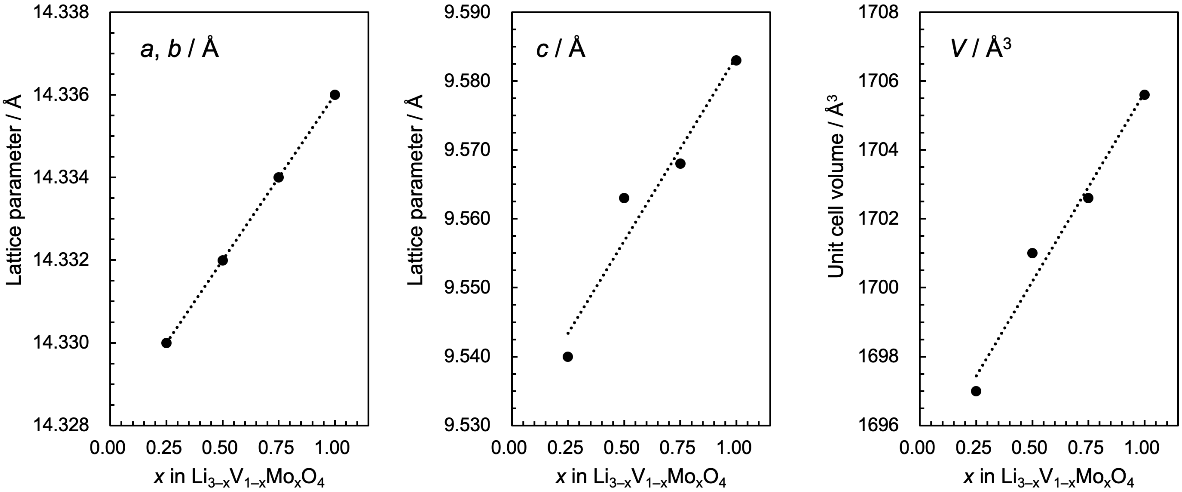

Figure S3. Shift of lattice parameters and unit-cell volume of spray-dried LVMoO powders. The parameters were obtained by full-pattern fitting of synchrotron XRD data for each composition. All parameters vary linearly with x (Mo content), consistent with Vegard's law, showing that spray-dried LVMoO forms an ideal solid solution across the nominal composition range. Detailed fitting results are provided in Table S1.

Table S1. Refined lattice parameters of spray-dried LVMoO powders (space group *R*-3). Values of *a*, *b*, *c*, and unit-cell volume *V* were obtained by full-pattern fitting of synchrotron XRD data. The quality indicators of the fits (R_{wp} and *S*) are also listed. Reference pattern: ICDD #01-070-8448.

x	a, b / Å	c / Å	V / Å^3	R_{wp} / %	S / -
1	14.336(4)	9.583(3)	1705.6(9)	12.63	1.2274
0.75	14.334(5)	9.568(3)	1702.6(10)	8.49	0.7493
0.50	14.332(14)	9.563(10)	1701(3)	10.86	0.8399
0.25	14.33(4)	9.54(3)	1697(7)	16.75	1.1098

S.G.: *R*–3 (148)

Reference: ICDD #01-070-8448

Local coordination structure probed by EXAFS

To further examine the local coordination environment in the solid-solution series, EXAFS analyses at the Mo K-edge and V K-edge were performed for powder samples with different compositions (Figure S4). The results indicate that the local structure is generally well maintained across the series, supporting that the solid-solution phase is formed without severe local structural collapse or obvious nanoscale phase separation. In particular, the Mo K-edge EXAFS and the corresponding radial distribution functions are consistent with Mo being accommodated in a reasonably well-defined tetrahedral local environment. These results support the view that the spray-dried LVMoO samples preserve a sound local coordination framework even in the metastable solid-solution state.

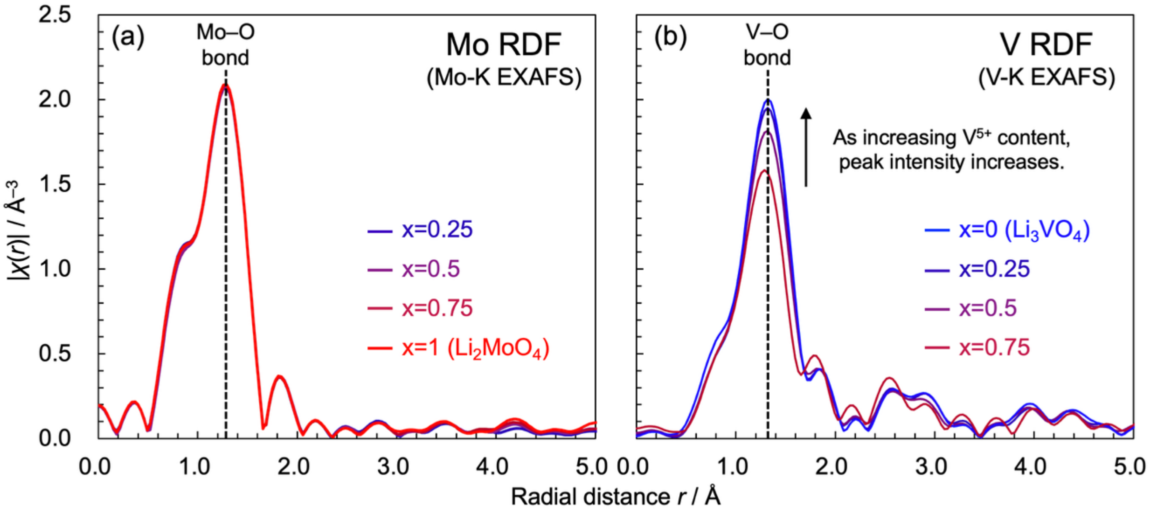

Figure S4. Fourier-transformed EXAFS spectra (radial distribution functions; RDF) at (a) Mo K-edge and (b) V K-edge for $Li_{3-x}V_{1-x}Mo_xO_4$ ($0 \le x \le 1$). The Mo–O peak shows little change with composition, while the V–O peak becomes sharper and increases in intensity with increasing V content.

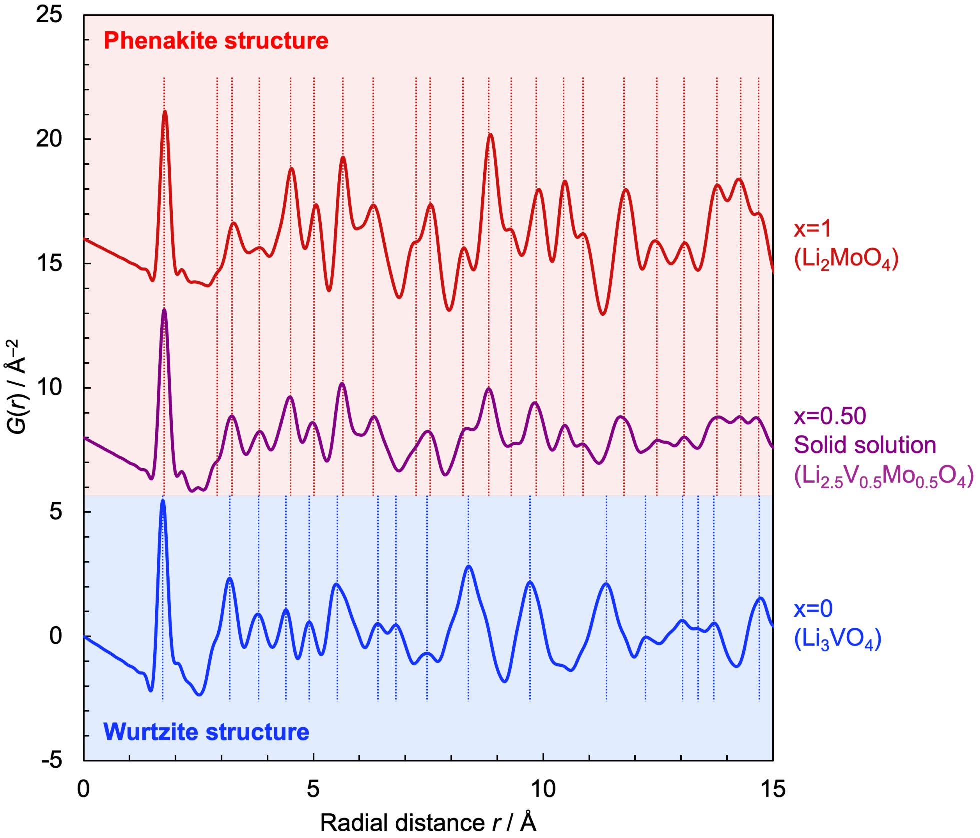

Figure S5. Pair distribution function (PDF) profiles of $Li_{3-x}V_{1-x}Mo_xO_4$ for x = 0, 0.50, and 1. The end members show distinct local structures corresponding to wurtzite-type (x = 0) and phenakite-type (x = 1) frameworks. The intermediate composition (x = 0.50) closely follows the PDF profile of x = 1 over the entire *r*-range, without additional features attributable to secondary phases or amorphous components, indicating a single-phase phenakite-type solid solution.

Simulated droplet drying behavior during spray drying

First, we clarify the drying kinetics and concentration evolution. To provide a quantitative estimate, we modeled the droplet evaporation using the D^2-law (Equation S1):

$$D^2(t) = D_0^2 - K\,t \qquad \text{(Equation S1)}$$

where D_0 is the initial droplet diameter, $D(t)$ [m] is the instantaneous droplet diameter, K [$\mathrm{m^2\ s^{-1}}$] is the evaporation rate constant, and t [s] is the drying time. For an aqueous droplet with D_0 = 100 µm in a 160 °C drying gas, K is estimated to be approximately $1.19 \times 10^{-8}\ \mathrm{m^2\ s^{-1}}$. Assuming ideal shrinkage, the droplet would completely evaporate in a theoretical time t_e of approximately 0.84 s.

The evaporation rate constant K was estimated based on the heat-transfer controlled evaporation model for a spherical droplet (Nusselt number $Nu \approx 2$), expressed as $K = 8k_g(T_g - T_w) / (\rho_l\,\Delta H_v)$. Here, k_g is the thermal conductivity of the surrounding air (~0.03 $\mathrm{W\ m^{-1}\ K^{-1}}$), T_g is the drying gas temperature (160 °C), T_w is the wet-bulb temperature of the droplet (~48 °C), ρ_l is the density of water (1 $\mathrm{g\ cc^{-1}}$), and ΔH_v is the latent heat of vaporization of water (~$2.26 \times 10^6\ \mathrm{J\ kg^{-1}}$).

Under these conditions, the internal concentration $C(t)$ increases proportionally to the inverse cube of the droplet diameter $D(t)$, causing the supersaturation ratio $S(t)$ to spike exponentially in the final fraction of a second.

$$C(t) = C_0(D_0/D(t))^3 \qquad \text{(Equation S2)}$$

$$S(t) = C(t)/C_{eq} \qquad \text{(Equation S3)}$$

We have visualized these kinetics. As shown in Figure S6, the droplet diameter $D(t)$ decreases as an inverse of a quadratic function within 0.84 s. Crucially, the internal concentration $C(t)$ and the supersaturation ratios ($S_V(t)$, $S_{Mo}(t)$) exhibit exponential rise in the very final stage of drying. Based on our initial precursor solution concentration of C_0 = 0.0737 M, we can calculate the exact timing of precipitation by substituting C_{eq} into the aforementioned equations. The V species reach their precipitation threshold $C_{eq\text{-}V}$ (~0.3 M) at t = 0.51 s. Subsequently, the Mo species reach their threshold $C_{eq\text{-}Mo}$ (~3 M) at t = 0.77 s. In the ideal continuous shrinkage model, the time gap between the onset of V and Mo precipitation is 0.26 s. As a result, phase separation is unlikely on such an ultrashort timescale.

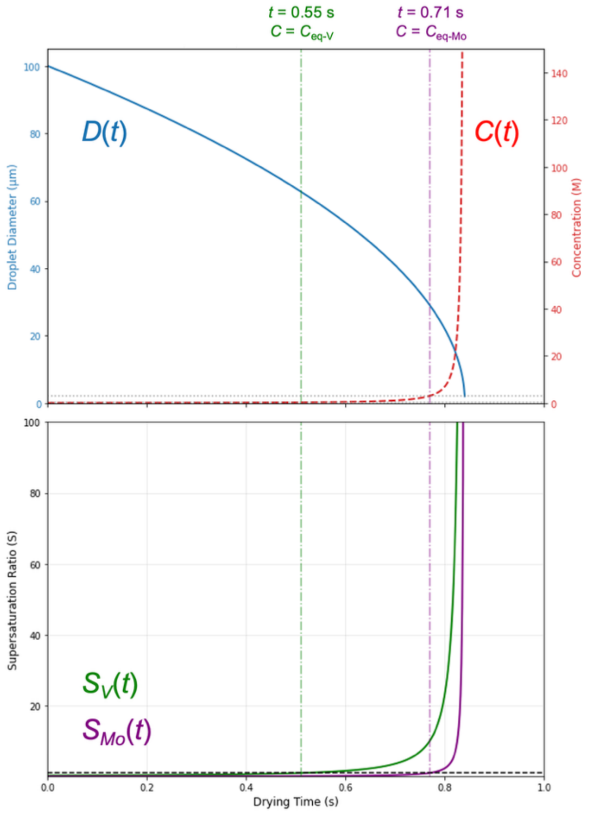

Figure S6. Simulated droplet evaporation kinetics during the spray drying process. (Top) Evolution of the droplet diameter $D(t)$ and internal concentration $C(t)$ over time. (Bottom) Supersaturation ratios $S(t)$ for V and Mo species. Vertical lines indicate the precipitation onset (S = 1) for V at 0.55 s and Mo at 0.77 s. This exponential spike in supersaturation within a fraction of a second restricts crystal growth and accelerates nucleation, driving the near-simultaneous co-precipitation of both species.

In the conventional sol-gel process, 100 mL of precursor solution requires approximately 3 h (~10^4 s) to dry. This corresponds to a difference in drying time by more than four orders of magnitude compared to the spray-drying process. This slow process allows V species to nucleate and precipitate long before Mo species, leading to severe phase separation.

Furthermore, we acknowledge that the real precipitation kinetics deviate from this ideal continuous shrinkage model. In reality, simultaneous precipitation consumes solutes and should subsequently lower the liquid phase concentration. The exact concentration profile depends heavily on balance between the precipitation rate and the evaporation rate. Additionally, the formation of a solid shell significantly alters the mass-transfer dynamics before and after its formation. Therefore, while the simulation presented here relies on a simplified model, it qualitatively demonstrates the dynamics of the sub-second evaporation and the sharp concentration rise of spray-dried droplets. We have added these detailed discussions and the simulation to the Supplementary Information and revised the main text to cite this mechanism.

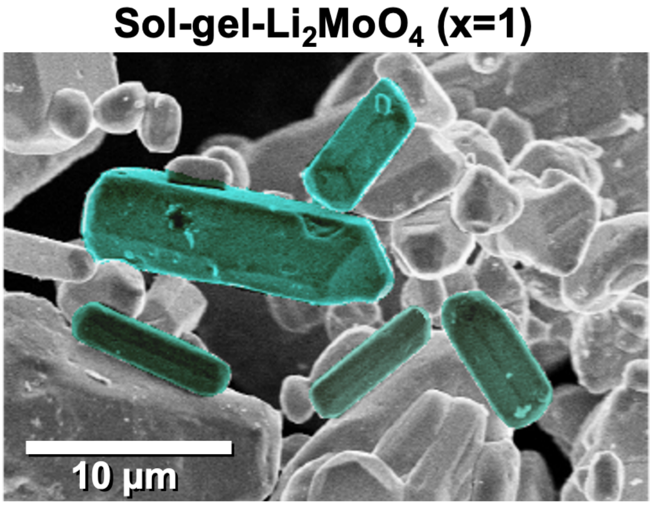

Figure S7 SEM image of the sol-gel synthesized Li_2MoO_4 (x=1) powder sample, displaying large faceted hexagonal rod-shape crystals with 10–30 µm in length.

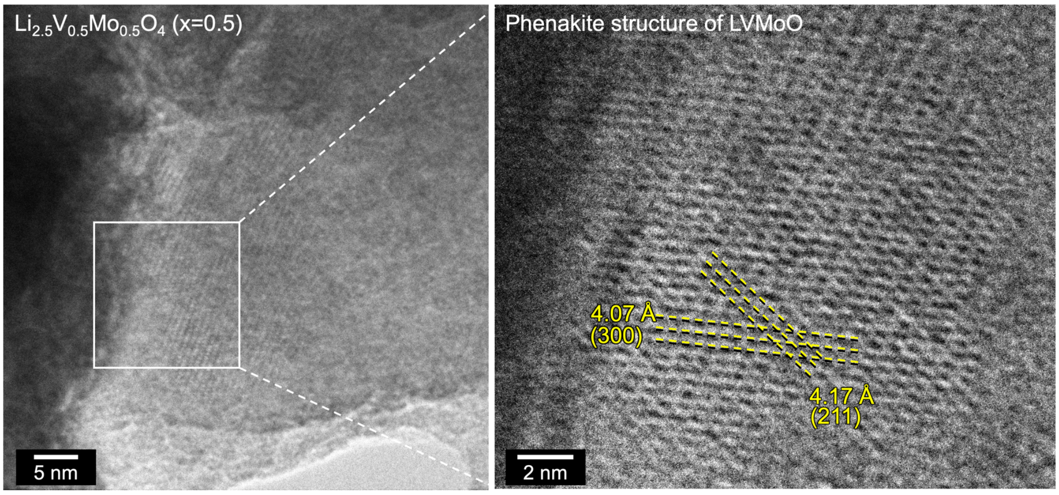

Figure S8. High-resolution TEM images of the $Li_{3-x}V_{1-x}Mo_xO_4$ sample at x = 0.50. The enlarged image shows clear lattice fringes with interplanar spacings consistent with the phenakite-type structure, confirming the formation of a well-defined crystalline phase at the nanoscale.

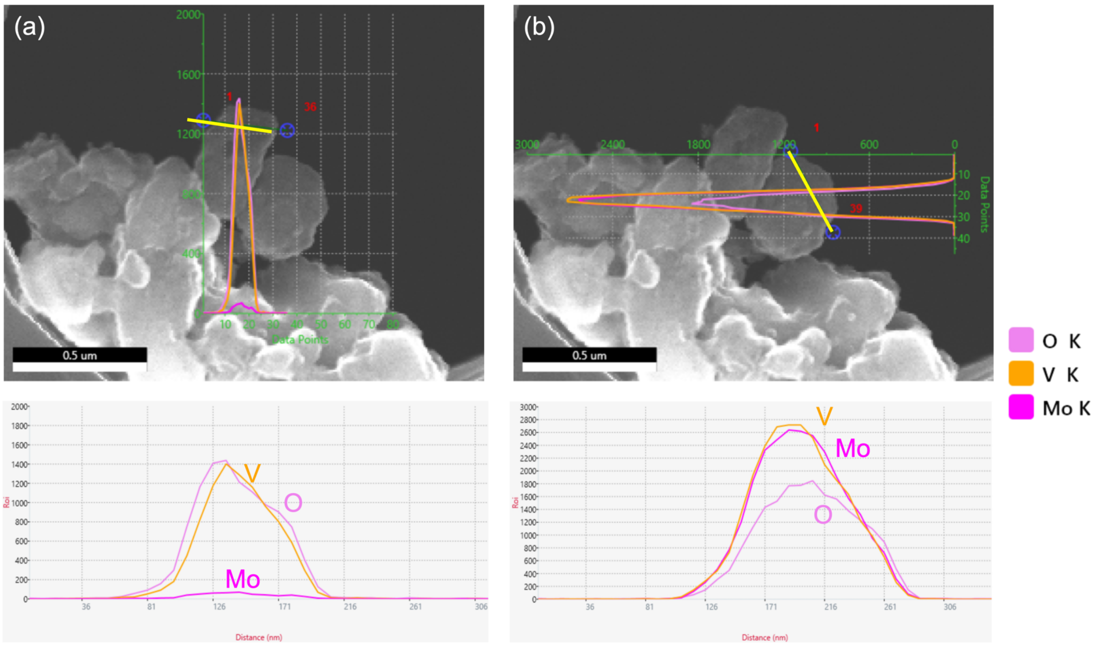

Figure S9. SEM images with EDS line-scan profiles of x=0.50 LVMoO particles. (a) Local scan showing co-distribution of V and O with weaker Mo signal. (b) Local scan across a different particle showing relatively uniform distribution of V, Mo, and O. Bottom panels show corresponding intensity profiles.

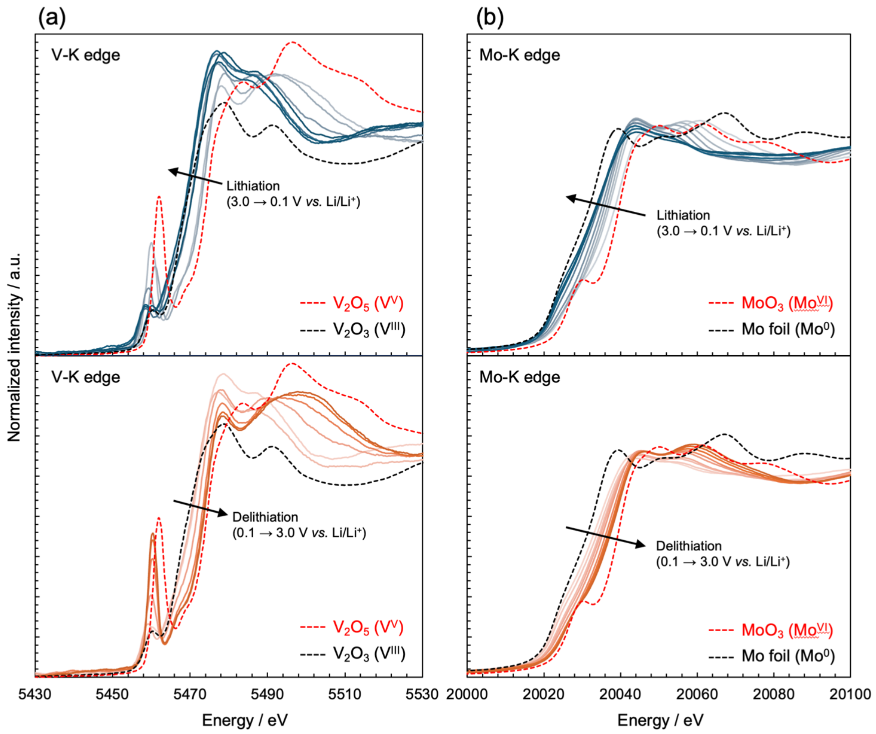

Figure S10. *In-situ* XAFS analysis of $Li_{3-x}V_{1-x}Mo_xO_4$ (x = 0.50) at the Mo K-edge and V K-edge during lithiation and delithiation. The Mo absorption edge shifts toward lower energy during lithiation, approaching a state close to metallic Mo, and reversibly returns upon delithiation. Similar reversible behavior is observed at the V K-edge.

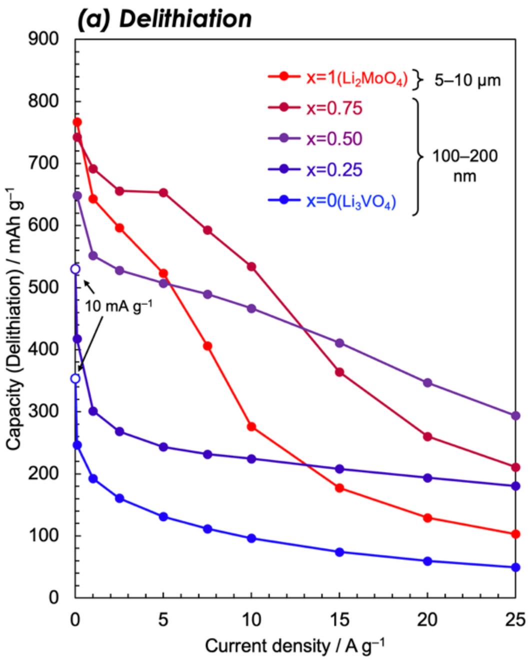

Figure S11. Rate performance of Li$_{3-x}$V$_{1-x}$Mo$_x$O$_4$ electrodes for x = 0, 0.25, 0.50, 0.75, and 1 during (a) delithiation and (b) lithiation. Size of the primary particle, which were observed by SEM images (Figure 3), are shown together with the legends.

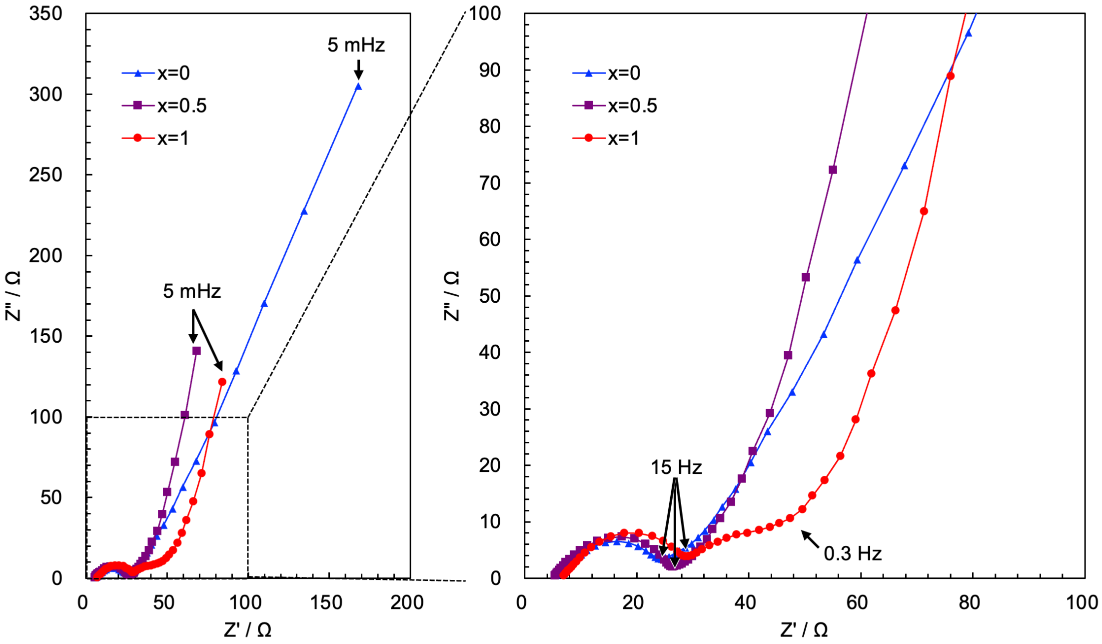

Figure S12. Nyquist plots of representative Li$_{3-x}$V$_{1-x}$Mo$_x$O$_4$ electrodes (x = 0, 0.5, and 1) measured at 0.4 V. The enlarged view highlights the high- to middle-frequency region, where no major difference is observed in the semicircle associated mainly with charge-transfer-related processes. In contrast, clearer differences appear in the low-frequency region: x = 1 shows an additional depressed arc-like response, whereas x = 0 exhibits a long sloping tail, indicating distinct low-frequency kinetic behavior depending on composition and morphology.

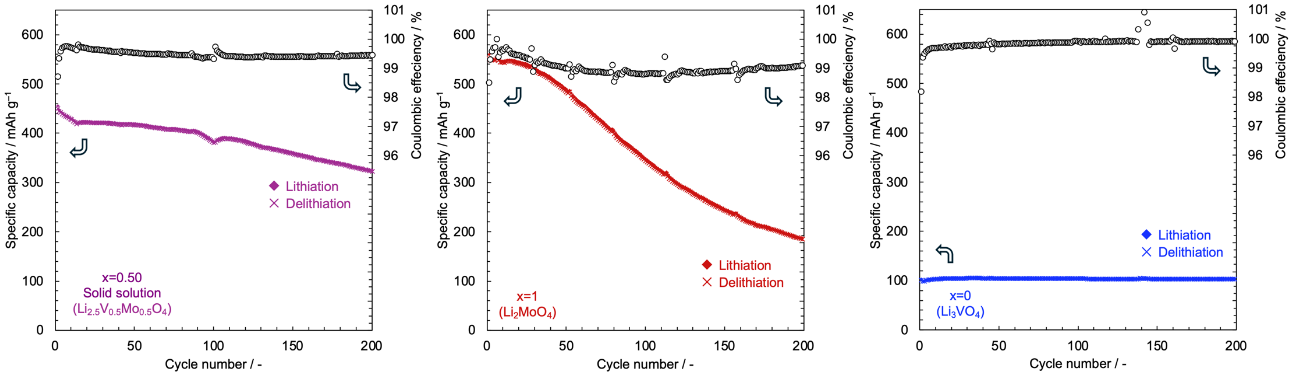

Figure S13. Cycling performance and corresponding coulombic efficiency of $Li_{3-x}V_{1-x}Mo_xO_4$ electrodes for x = 0, 0.50, and 1. All samples exhibit high coulombic efficiency (>99%) during cycling, while differences in capacity retention are observed among compositions.

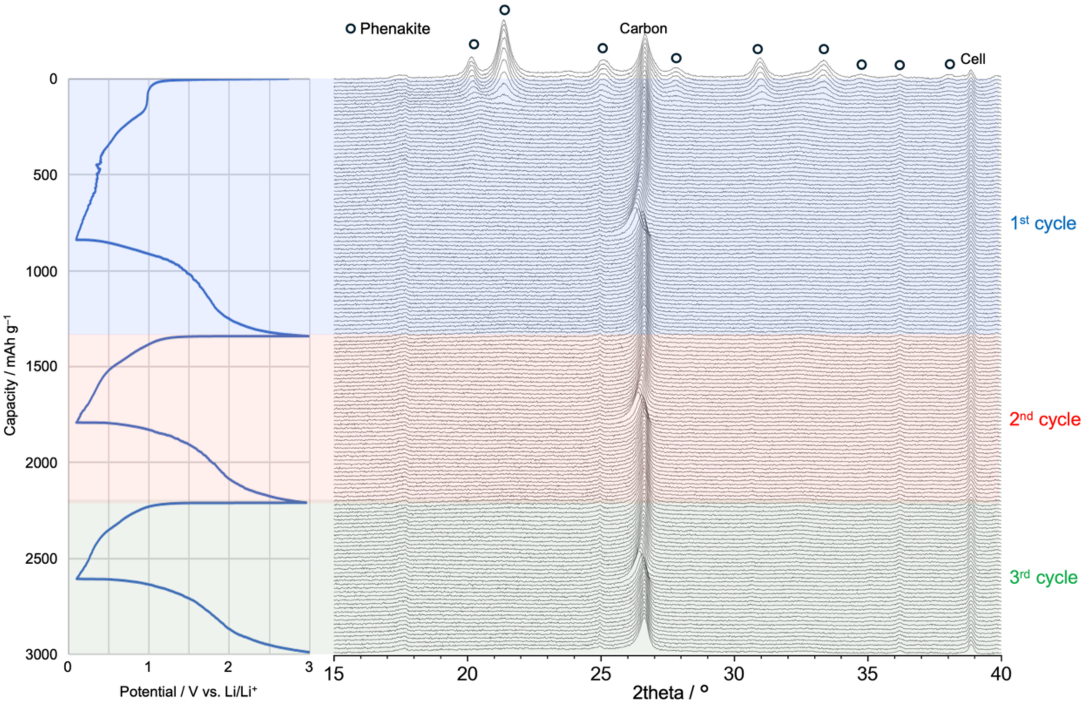

Figure S14. *In-situ* XRD patterns of Li$_{3-x}$V$_{1-x}$Mo$_x$O$_4$ (x = 0.50) during three lithiation/delithiation cycles. The diffraction peaks are strongly attenuated during lithiation, indicating a marked loss of long-range crystallinity under deep lithiation. This behavior is reproducibly observed over repeated cycles.

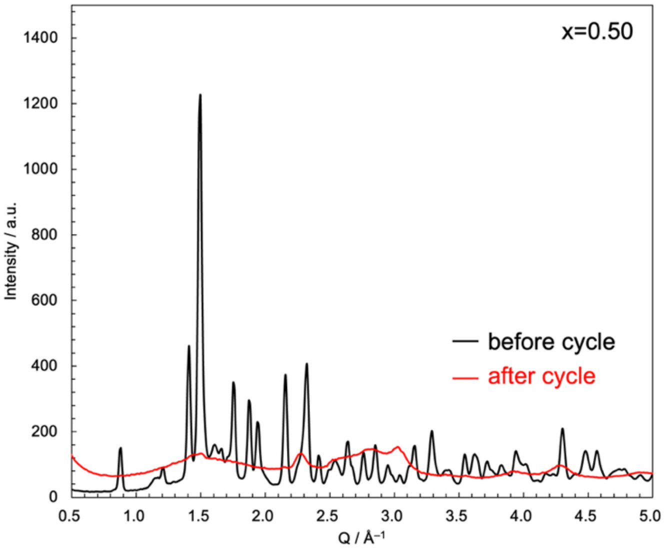

Figure S15. Synchrotron X-ray diffraction patterns of Li$_{3-x}$V$_{1-x}$Mo$_x$O$_4$ (x = 0.50) before and after electrochemical cycling. After lithiation, the diffraction peaks are significantly broadened and reduced in intensity, indicating loss of long-range crystallinity. No distinct reflections corresponding to crystalline metallic Mo phases are observed.

Table S2. Comparison of electrochemical performance and synthesis features of representative Li_3VO_4-, Li_2MoO_4-, and related high-rate oxide anodes for Li-ion storage.

Material	Synthesis / structural feature	Carbon coating / composite	Low-rate capacity	Rate performance	Cycling stability	Loading mass	Year	Ref.
Spray-dried $Li_{2.5}V_{0.5}Mo_{0.5}O_4$	Spray drying; supersaturated solid solution; 120 nm particles	-	650 mAh g^{-1} @0.1A g^{-1}	411 mAh g^{-1} @15.0 A g^{-1} (delithiation) 326 mAh g^{-1} @5.0 A g^{-1} (lithiation)	71% @200th	1.5 mg cm^{-2}	2026	This work
PEDOT:PSS-coated Li_3VO_4	Surface polymer modification of LVO	conductive-polymer coat	383.6 mAh g^{-1} @ 0.2 A g^{-1}	191.9 mAh g^{-1} @3.152 A g^{-1}	97.4% @2000th	-	2023	S-C. Hsu et al. [1]
$LiNbO_3$-coated Li_3VO_4	One-pot sol–gel; nanosized LVO with $LiNbO_3$ surface layer	$LiNbO_3$ surface coating	534 mAh g^{-1} @ 0.06 A g^{-1}	230 mAh g^{-1} @1.6 A g^{-1}	87% @200th	1.5 mg cm^{-2}	2024	E. Elmaataouy et al. [2]
Cr-doped and carbon-coated Li_3VO_4	MOF-derived; Cr^{3+} doping; oxygen-defect-containing LVO	Carbon coating	397.0 mAh g^{-1} @ 0.04 A g^{-1}	282.0 mAh g^{-1} @3.94 A g^{-1}	80.4% @200th	-	2025	C-C. Lu et al. [3]
Carbon-coated Li_2MoO_4	Thermal polymerization	Carbon coating	669 mAh g^{-1} @ 0.09 A g^{-1}	255 mAh g^{-1} @1.8 A g^{-1}	65% @60th	-	2016	H-Y. Wang et al. [4]
Carbon-coated Li_2MoO_4 hollow nanotubes	Sol–gel	Carbon coating	600 mAh g^{-1} @ 0.09 A g^{-1}	200 mAh g^{-1} @0.7 A g^{-1}	75% @60th	3 mg (no area data)	2014	X. Liu et al. [5]
$Nb_{14}W_3O_{44}$	Solvothermal-derived precursor + sintering	-	226 mAh g^{-1} @ 0.04 A g^{-1}	137 mAh g^{-1} @6.0 A g^{-1}	74.2% @1000th	-	2021	X. Huang et al. [6]
$W_{0.1}Ti_{0.9}Nb_2O_7$	Acidified H_2O_2-assisted spray drying + calcination at 750 °C; porous spherical nanomaterial	-	266.0 mAh g^{-1} @ 0.04 A g^{-1}	167.7 mAh g^{-1} @7.752 A g^{-1}	93.4% @250th	6 mg cm^{-2}	2025	J. Li et al. [7]
Mn0.1-TiNb2O7 @rGO/CNT	Carbon compositing Mn-dope	Carbon compositing	270 mAh g^{-1} @ 0.5C	175 mAh g^{-1} @ 30C	70% @1000th	1 mg cm^{-2}	2025	L. Huang et al. [8]
rGO/$Nb_{16}W_5O_{55}$	rGO-coated $Nb_{16}W_5O_{55}$	rGO coating	257 mAh g^{-1} @ 0.03 A g^{-1}	116 mAh g^{-1} @13.6 A g^{-1}	92.7% @500th	1-3 mg cm^{-2}	2025	Y. Guo el al. [9]
DRX-$Li_3V_2O_5$	Electrochemically induced disordered rock-salt $Li_{3+x}V_2O_5$ anode	-	266 mAh g^{-1} @ 0.10 A g^{-1}	109 mAh g^{-1} @20.0 A g^{-1}	>90% @1000th	2-3 mg cm^{-2}	2020	H. Liu et al. [10]
DRX-$Na_{0.6}Li_{2.4}V_2O_5$ @PANI composite	Stepwise lattice tailoring; PANI pre-intercalation + Na+ doping	PANI composite / conductive polymer	230 mAh g^{-1} @ 0.10 A g^{-1}	150 mAh g^{-1} @10.0 A g^{-1}	94% @1000th	5 mg cm^{-2}	2023	Z. Wang et al. [11]

References

1. S. C. Hsu, K. S. Wang, Y. T. Lin, J. H. Huang, N. J. Wu, J. L. Kang, H. C. Weng and T. Y. Liu, *Polymers*, 2023, **15**, 2502.
2. E. Elmaataouy, A. Chari, A. Al-Shami, G. Elomari, M. Aqil, J. Gim, R. Amine, H. Martinez, J. Alami, O. Mounkachi and M. Dahbi, *Journal of Energy Storage*, 2024, **86**, 111351.
3. C. C. Lu, H. F. Lin, J. H. Huang, Y. C. Yen, W. K. Pang, H. C. Weng, S. C. Hsu and Z. L. Tseng, *Journal of Energy Storage*, 2025, **136**, 118390.
4. H. Y. Wang, B. K. Zou, Z. F. Tang, Z. Y. Wen and C. H. Chen, *Mater. Lett.*, 2016, **177**, 54-57.
5. X. Liu, Y. Lyu, Z. Zhang, H. Li, Y. S. Hu, Z. Wang, Y. Zhao, Q. Kuang, Y. Dong, Z. Liang, Q. Fan and L. Chen, *Nanoscale*, 2014, **6**, 13660-13667.
6. X. K. Huang, W. Y. Zhou, X. W. Chen, C. H. Jiang and Z. M. Zou, *Electrochim. Acta*, 2021, **368**, 137613.
7. J. G. Li, L. Y. Hao, X. Y. Han, G. Y. Wei, J. W. Yu, L. Zhang, Y. Li, L. Wang and X. M. He, *Electrochim. Acta*, 2025, **537**, 146838.
8. L. Huang, Y. Huang, J. Wang, J. Lin, J. Xu, Z. Yin, X. Wang, M. Li, X. Shi, L. Shao and Z. Sun, *ACS Applied Materials & Interfaces*, 2025, **17**, 53659-53669.
9. Y. Guo, C. Guo, P. Li, W. Song, W. Huang, J. Yan, X. Liao, K. He, W. Sha, X. Zeng, X. Tang, Q. Ren, S. Wang, K. Amine, A. Nie, T. Liu and Y. Yuan, *Nat Commun*, 2025, **16**, 2441.
10. H. Liu, Z. Zhu, Q. Yan, S. Yu, X. He, Y. Chen, R. Zhang, L. Ma, T. Liu, M. Li, R. Lin, Y. Chen, Y. Li, X. Xing, Y. Choi, L. Gao, H. S. Cho, K. An, J. Feng, R. Kostecki, K. Amine, T. Wu, J. Lu, H. L. Xin, S. P. Ong and P. Liu, *Nature*, 2020, **585**, 63-67.
11. Z. Wang, S. Yuan, X. Tang, H. Wang, M. Zhang, F. Liu, N. Yao and Y. Ma, *Energy Storage Materials*, 2023, **54**, 284-293.